Evaluating the performance of efficient Cu$_2$NiSnS$_4$ solar cell—A two stage theoretical attempt and comparison to experiments

Most. Marzia Khatun, Adnan Hosen, Sheikh Rashel Al Ahmed [*]

Department of Electrical, Electronic and Communication Engineering, Pabna University of Science and Technology, Pabna 6600, Bangladesh

A R T I C L E   I N F O

A B S T R A C T

In this work, copper nickel tin sulfide (Cu$_2$NiSnS$_4$) as an encouraging alternative absorber for thin-film photovoltaic devices is explored. Here, the Cu$_2$NiSnS$_4$ (CNTS) absorber-based heterojunction solar cell is designed through a two-stage theoretical approach using Solar Cell Capacitance Simulator in one-dimension (SCAPS-1D). Initially four different hole transport materials (MoO$_3$, SnS, NiO$_x$, and PEDOT.PSS) are incorporated at the back interface in experimentally configured Au/Cu$_2$NiSnS$_4$/ZnS/ZnO/ITO cell to boost the device outputs. The MoO$_3$ semiconductor is anticipated as a hole transport layer (HTL) in the heterojunction Ni/MoO$_3$/Cu$_2$NiSnS$_4$/ZnS/ZnO/ITO solar configuration. It is revealed that an appropriate band alignment can be formed at MoO$_3$/Cu$_2$NiSnS$_4$ interface with less interfacial defects among other HTLs with CNTS absorber, thus improving the solar cell outputs. Efficiency is increased from 2.71% to 8.79% for the proposed CNTS-based solar cell. Further optimization is accomplished concerning thickness, defect states, and doping density of the various materials utilized in the heterojunction structure. Defect characteristics at the MoO$_3$/Cu$_2$NiSnS$_4$ and Cu$_2$NiSnS$_4$/ZnS interfaces are also evaluated and optimized to boost the conversion efficiency significantly. Moreover, the effects of operating temperature and rear electrode work function on the outputs of the designed solar device are studied. The aforesaid two-stage optimization yields efficiency of 12.46% with V$_{OC}$ of 1.23 V, J$_{SC}$ of 12.66 mA/cm^2, and FF of 79.78%. Therefore, these findings will facilitate the scientific communities to further progress an economical and extremely efficient CNTS-based solar device with a promising MoO$_3$ HTL.

1. Introduction

The utmost plentiful and cleanest renewable energy source among others is solar energy. Photovoltaic technologies are being used as one of the main approaches to harness the solar energy at large scales [1–4]. Silicon has been used to develop the mainstream of nowadays solar devices because it offers moderate prices and decent power conversion efficiency (PCE) [5–7]. However, high fabrication expense with high-temperature processing of the silicon (Si) wafers limits the mass production of the Si-based photovoltaic (PV) cells. Thin-film solar cells (TFSCs) utilizing semiconductor material-based very thin layers have much attracted in the scientific community for applications of the PV technology [8–12]. There are numerous benefits of the thin-film heterojunction PV devices such as excellent flexibility, lightweight, remarkable electrical and optical features, ease of scaling than the process flow needed by the silicon-based PV structures, low production costs, and high PCE [8,9,13–15].

---

* Corresponding author.
  E-mail address: rashel@pust.ac.bd (S.R.A. Ahmed).

In recent years, the quaternary chalcogenide semiconductor Cu_2NiSnS_4 (CNTS) thin-films [16–19] have been widely investigated for the solar energy transformation as potential alternatives to the silicon [20], cadmium telluride (CdTe) [21] and $Cu(In,Ga)Se_2$ (CIGS) [22,23] thin-films containing rare-earth and toxic materials. Several privileges including suitable energy gap ranged from 1.45 to 1.74 eV, significant absorption coefficient ($>10^4$ cm^{-1}), inexpensive and enormous earth-abundant elements, low toxicity, and reasonably extensive steadiness make the p-type CNTS semiconductor material effective as a promising absorber in the TFSC [24–30]. Several techniques such as spray sandwich method [31], electrodeposition post-sulfurization [26,32], direct solution coating post-sulfurization [28], and facile synthesis method [33] have been used to fabricate the CNTS films for the solar cell applications. Very recently, a spin-coating method has been employed to prepare the CNTS thin-film without sulfurization [34]. In the earlier works, a number of experimental studies have been discussed to realize the highly efficient and low-cost heterojunction CNTS-based TFSCs [27, 35–37]. An experimental conversion efficiency of 0.09% with short-circuit current density (J_{SC}) of 0.52 mA/cm^2, open-circuit voltage (V_{OC}) of 0.42 V, and fill-factor (FF) of 43% is obtained for the CNTS-based TFSC with a configuration of glass/-Mo/CNTS/CdS/Al–ZnO/Al [35]. In the previous practical approach, the researchers have reported the PCE of 2.71% with $J_{SC} = 6.82$ mA/cm^2, $V_{OC} = 0.75$ V, and FF = 53.10% for the TFSC with the architecture of Au/CNTS/ZnS/ZnO/ITO [27]. The conversion efficiency of 0.64 % including $J_{SC} = 3.1$ mA/cm^2, $V_{OC} = 0.62$ V, and FF = 33.5% is also obtained for the CNTS device [36]. It has been presented that a PV efficiency of 11.34 % with other device parameters such as $J_{SC} = 18.96$ mA/cm^2, $V_{OC} = 0.56$ V, and FF = 53% can be attained for the fabricated CNTS-based device [37]. Nevertheless, the practically obtained PCE of the CNTS absorber-based thin-film solar cell cannot race with the existing TFSC modules. It can be realized that the PCE evaluated experimentally is still insufficient according to the predictable efficiency approximately 33% for the CNTS absorber having band gap from 1.4 to 1.7 eV by the Shockley–Queisser limit [38]. In this sense, the heterojunction CNTS TFSC has modified theoretically to enlarge the PV performances [39,40].

In the former study, the enhanced efficiency of the modified CNTS-based TFSC structure of Cu_2O/CNTS/ZnS/ZnO/ITO has been reported to be 4.60% with a $J_{SC} = 6.44$ mA/cm^2, $V_{OC} = 1.03$ V, and FF = 69.27 %, where the Cu_2O is exploited as a hole transport layer (HTL) at the back of the CNTS absorber [39]. In addition, a theoretical PCE of 17.06% is found for the PV device of CNTS/ZnS/Zn(O, S)/FTO introducing the ZnS/Zn(O,S) stacked electron transport layers [40]. According to the theoretical efficiency limit, the efficiencies reported earlier are not good enough. The major issues for the poor conversion efficiency are carrier recombination, energy band discontinuity, and deficient interface quality owing to existence of defects in the thin-film heterojunction PV devices [41–43]. Therefore, further modifications into the CNTS thin-film PV devices with optimization of material parameters are necessary to boost the overall solar cell output parameters.

To enhance the device outputs, in the former reports, several electron reflectors or HTLs at the rear side in the heterojunction PV cell have been introduced [44–50]. It has been suggested that an appropriate potential height by adding an HTL amid an absorber and a back electrode may minimize the surface recombination loss at the back surface [39,41,44,51]. It is also expected that a low valence band offset (VBO) at the HTL/absorber interface will be effective to ease flow of carriers (holes) from the absorber to the rear electrode through HTL. Furthermore, the overall device cost can be lessened by decreasing the absorber area with adding an HTL at the rear side [43,49,50,52].

To achieve a highly efficient PV cell with superior device parameters, in this research, four various HTLs such as the MoO_3 [53], SnS [54,55], NiO_x [56,57], and PEDOT.PSS [58] have been introduced into a standard CNTS solar cell structure of Au/CNTS/ZnS/Z-nO/ITO [27]. Herein, the p$^+$ MoO_3 semiconductor as a suitable HTL is added to the reference CNTS heterojunction TFSC. The MoO_3 has interested as a promising material for the PV device applications. This is because there are excellent optoelectronic aspects including appropriate energy band gap (E_g) with sufficient work function, high mobility, elongated diffusion distance, low harmfulness, high stability, plentiful constituents in the globe, and less expensive [53]. The MoO_3 can be utilized as a most encouraging HTL among the suggested other HTLs due to large positive conduction band offset (CBO) and smaller valence band offset (VBO) values determined with the CNTS absorber [39,53], thereby ensuring efficient carrier moving to the rear side electrode from the CNTS absorber with suitable band alignment at the back interface. Moreover, a smaller lattices mismatch amid the MoO_3 HTL and CNTS absorber than the other HTLs with the CNTS layer will provide less interfacial defects and recombination at the back interface [31,59], thus enhancing the overall PV performances.

In this study, a novel heterojunction Ni/MoO_3/Cu_2NiSnS_4/ZnS/ZnO/ITO PV configuration is proposed, where the MoO_3 material is introduced as an HTL. Initially, the conventional CNTS-based thin-film PV device structure of Au/CNTS/ZnS/ZnO/ITO reported practically is simulated to check the reliability of this numerical investigation on the proposed CNTS TFSC with HTL. This numerical works have been performed by operating the widely used SCAPS-1D simulation tool. We have evaluated an optimal efficiency by optimizing several material properties such as thickness, doping density, and defect densities in the bulk material as well as at interfaces. In addition, the impacts of functioning temperature and rear electrode work function on the device outputs have been investigated.

2. Methodology and materials

2.1. Numerical modeling

Numerical modeling through software program becomes useful for good perspective to understand physical mechanisms of a complex solar cell structure. Herein, the SCAPS-1D software package [60,61] is utilized as a simulation tool to evaluate the CNTS-based TFSCs. The operation of the SCAPS-1D simulator includes explaining the elementary semiconductor equations (1)–(3): Poisson equation, electron and hole continuity equations at each position of the device maintaining the boundary conditions, and the
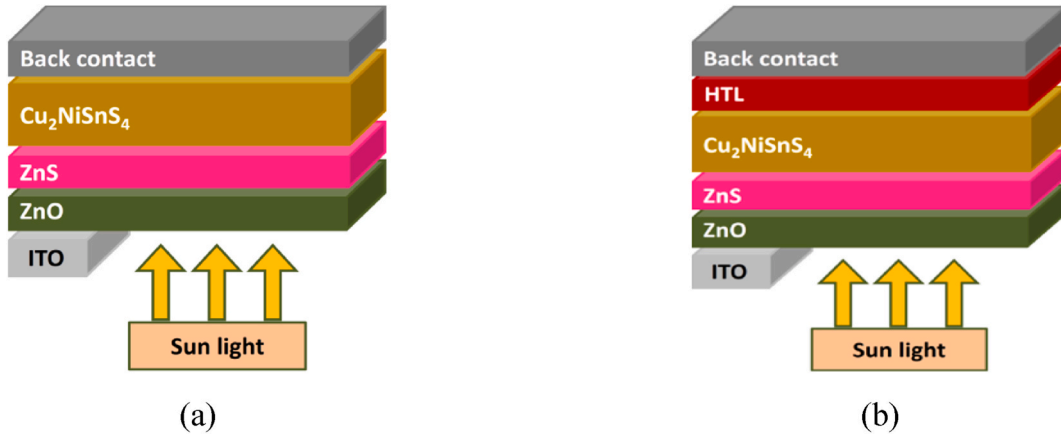
Fig. 1. CNTS solar cell structures: (a) baseline cell and (b) proposed cell with HTL.

Table 1

Parameters used to check validity with experimental work [25,27].

Parameters	n^+-type ETL (ZnO)	n-type Buffer (ZnS)	p-type Absorber (CNTS)
Thickness, W (μm)	0.2	0.2	1.0
Bandgap, E_g (eV)	3.3	3.4	1.74
Electron affinity, χ (eV)	4.3	4.1	3.87
Permittivity (relative), ε	9	9	9
Conduction band (CB) effective density of states (DOS) (cm^{-3})	2.2×10^{18}	2.2×10^{18}	2.2×10^{18}
Valence band (VB) effective DOS (cm^{-3})	1.8×10^{19}	1.8×10^{19}	1.8×10^{19}
Electron mobility, μ_n (cm^2/V-s)	100	100	11
Hole mobility, μ_p (cm^2/V-s)	25	25	11
Donor density, N_D (cm^{-3})	4×10^{18}	5×10^{16}	0
Acceptor density, N_A (cm^{-3})			10^{17}
Defect density, N_t (cm^{-3})	10^{16}	10^{16}	5×10^{15}
Interface defect parameters used in device simulation			
Parameters	CNTS/ZnS		
Defect type	Neutral		
Capture cross-section of electrons, σ_n (cm^2)	10^{-19}		
Capture cross-section of holes, σ_p (cm^2)	10^{-19}		
Reference for defect energy level E_t	above the highest E_v		
Energy with respect to reference (eV)	0.6		
Total density (cm^{-2})	4×10^{13}		

equations are as follows,

$$\frac{\partial}{\partial x}\left(\varepsilon_0\varepsilon\frac{\partial\Psi}{\partial x}\right) = -q\left(p - n + N_D{}^+ - N_A{}^- + \frac{\rho_{def}}{q}\right) \tag{1}$$

$$\frac{\partial n}{\partial t} = -\frac{\partial}{\partial x}J_n - U_n + G \tag{2}$$

$$\frac{\partial p}{\partial t} = -\frac{\partial}{\partial x}J_p - U_n + G \tag{3}$$

where ε is permittivity, ψ is electrostatic potential, and p (or n) is density of hole (or electron). N_D and N_A are donor and acceptor ion concentrations, respectively, where ρ_{def} is the charge states of defect. J_n (or J_p) is the electron (or hole) current density, U and G are recombination and generation of charge carriers, respectively. The SCAPS-1D also introduces the defect levels at bulk and interfaces and calculates recombination loss in the heterojunction structure [62]. The Shockley–Read–Hall (SRH) model provides recombination current for bulk defects and in case of interface defects or surface defects, an expansion of the SRH model is employed to determine number of carriers taking part in interface recombination process [62]. To realize a realistic solar cell, in this work, bulk defects are initiated in the layers and interface defects are incorporated at the interfaces in the heterojunction TFSC. The default air mass of AM1.5G standard with incident light intensity of 1000 W/m^2 is selected for the illumination and the temperature is adjusted at 300 K. For comparison with experimental cell output parameters, the HTL layers are not considered in the initial simulation.

Table 2
Material parameters utilized in this numerical study to optimize CNTS TFSC with HTL [25,27,28,39,53–58].

Parameters (unit)	n$^+$-type ETL (ZnO)	n-type Buffer (ZnS)	p-type Absorber (CNTS)	p$^+$-type HTL (MoO$_3$)	p$^+$-type HTL (SnS)	p$^+$-type HTL (PEDOT.PSS)	p$^+$-type HTL (NiO$_x$)
W (μm)	0.02–0.2	0.07–0.2	0.05–5.5	0.02–0.2	0.1	0.1	0.1
E$_g$ (eV)	3.3	3.4	1.74	3.0	1.61	2.2	3.6
χ (eV)	4.3	4.1	3.87	2.5	3.80	2.9	1.46
ε	9	9	9	12.5	13	12.5	11.7
CB effective DOS (cm^{-3})	2.2×10^{18}	2.2×10^{18}	2.2×10^{18}	2.2×10^{18}	2.2×10^{18}	2.2×10^{18}	2.2×10^{18}
VB effective DOS (cm^{-3})	1.8×10^{19}	1.8×10^{19}	1.8×10^{19}	1.8×10^{19}	1.8×10^{19}	1.8×10^{19}	1.8×10^{19}
μ$_n$ (cm^2/V-s)	100	100	11	25	25	2×10^{-2}	2.8
μ$_p$ (cm^2/V-s)	25	25	11	100	100	2×10^{-4}	2.8
N$_D$ (cm^{-3})	4×10^{18}	10^{14}–10^{18}	0	0	0	0	0
N$_A$ (cm^{-3})	–	0	10^{12}–10^{16}	10^{14}–10^{20}	10^{18}	10^{18}	10^{18}
N$_t$ (cm^{-3})	10^{16}	10^{16}	10^{12}–10^{16}	10^{15}	10^{15}	10^{15}	10^{15}

Table 3
Parameters used at interfaces in proposed CNTS TFSC with HTL.

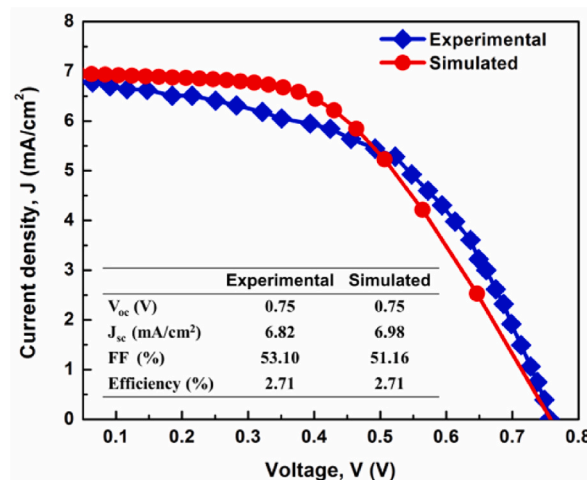| Parameters	CNTS/ZnS interface	MoO$_3$/CNTS interface
Defect type	Neutral	Neutral
Capture cross-section of electrons, σ$_n$ (cm^2)	10^{-12}-10^{-20}	10^{-12}-10^{-20}
Capture cross-section of holes, σ$_p$ (cm^2)	10^{-12}-10^{-20}	10^{-12}-10^{-20}
Reference for defect energy level E$_t$	above the highest E$_v$	above the highest E$_v$
Energy with respect to reference (eV)	0.6	0.6
Total density (cm^{-2})	10^{11}–10^{18}	10^{11}–10^{18}

Fig. 2. Comparison of simulation and experimental [27] J-V curves.

2.2. Device configuration and material properties

Fig. 1(a) and (b) reveal the simulated PV device. Initially, the reference CNTS solar cell organization composed of Au (back contact)/CNTS (absorber)/ZnS (buffer)/ZnO (electron transport layer or ETL)/ITO in Fig. 1(a) is simulated using parameters extracted precisely from an experimental CNTS-based PV device featuring the same materials represented in Table 1 [25,27]. On the other hand, the physical parameters extracted from previously reported studies used to optimize final Ni/MoO$_3$/CNTS/ZnS/ZnO/ITO device with HTL are illustrated in Table 2 [25,27,28,39,53–58]. Similar to experimental structure, Au and ITO have been used as back and front contacts, respectively. The electron and hole thermal velocities are assumed to be 10^7 cm/s. Defects with neutral type are deliberately added in the bulk layers and at HTL/absorber and absorber/buffer interfaces. Table 3 represents simulation parameters used at interfaces in the proposed CNTS-based TFSC with HTL.

The reproduced and experimental J-V curves of the CNTS solar cell are compared, as elucidated in Fig. 2. The cell outputs including
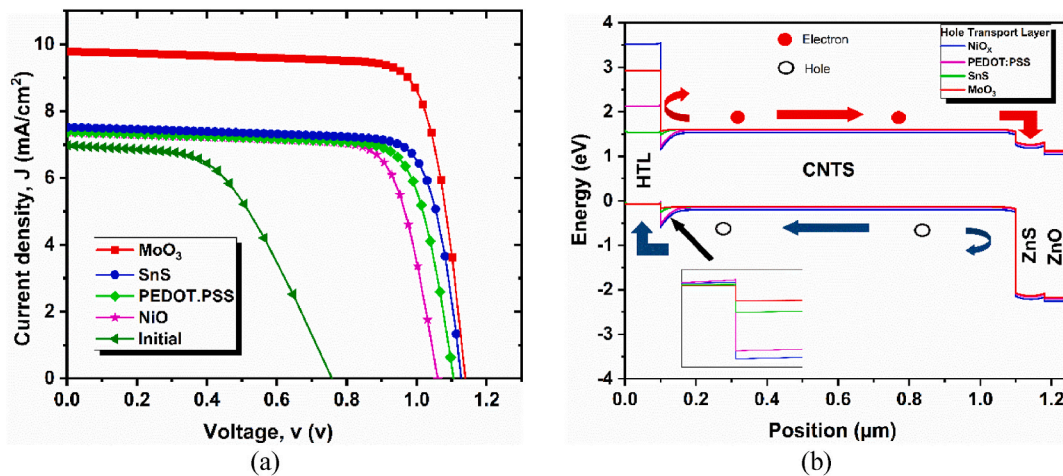
Fig. 3. (a) Comparison of J-V characteristics of initial device and configurations including different HTLs. (b) Energy band diagrams for CNTS solar cell including different HTLs.

V_{OC} of 0.75 V, J_{SC} of 6.98 mA/cm^2, FF 51.16%, and efficiency of 2.71% are obtained from the simulated J-V characteristics, on the other hand, the efficiency of 2.71 % with V_{OC} of 0.75 V, J_{SC} of 6.82 mA/cm^2, and FF 53.10% is found for the experimental CNTS solar cell [27]. It is identified that the PV outputs evaluated in this numerical analysis are approximately same as the reported experimental results. This excellent consistency between the simulation and experimental studies confirms the reliability of this simulation approach. Thus, to design and evaluate the heterojunction PV devices, the SCAPS-1D simulator can be efficiently utilized as a faithful numerical approach.

As mentioned in the introduction, the poor outputs of the conventional CNTS solar device may be due to low interface quality, thus leading to significant recombination loss in the heterojunction. An effective approach to diminish the recombination of charge carriers at the rear surface is to introduce an HTL at the back side of absorber [42,43,50]. To realize the highly efficient CNTS solar cell, in the present research, four different materials such as MoO$_3$, SnS, NiO$_x$, and PEDOT.PSS have been employed as HTLs in reference CNTS device and the resulting heterojunction Au/HTLs/CNTS/ZnS/ZnO/ITO TFSC schematic is exemplified in Fig. 1(b). The simulation parameters of various HTLs (MoO$_3$, SnS, NiO$_x$, and PEDOT.PSS) are obtained from the earlier researches [53–58] and are specified in Table 2. Also, the defect parameters defining absorber/HTL interface are provided in Table 3. The absorption co-efficient of the layers are calculated in the SCAPS-1D using the following equation [63], $\alpha = A_\alpha \sqrt{(h\nu - E_g)}$, where the pre-factor ($A_\alpha$) depends on the layers in the numerical calculation. In the present simulation study, the absorption coefficients of 1×10^5 cm^{-1} for ZnO, 5×10^5 cm^{-1} for ZnS, 1.5×10^4 cm^{-1} for CNTS, and 1×10^5 cm^{-1} for MoO$_3$ have been used, respectively.

3. Results and discussion

The simulation process in this paper is carried out in two steps. Firstly, we have simulated reference Au/CNTS/ZnS/ZnO/ITO structure without HTL as shown in Fig. 1(a). After evaluation of the numerical results compared to experimental reports, a suitable HTL is added to the conventional configuration revealed in Fig. 1(b) to attain high efficiency. Next, different numerical studies are performed to advance the device performance by optimizing the important parameters of the proposed CNTS PV structure.

3.1. Impact of HTLs on PV performances of CNTS solar cell

As the Au/CNTS/ZnS/ZnO/ITO heterojunction is formed, at steady state, the Fermi levels of entire films align and all the energy bands assemble correspondingly. In terms of carrier collection at the metal contacts, the primary issue of the CNTS-based thin-film PV structure is energy band discontinuity that may increase interfacial recombination loss at the rear surface. To reduce the recombination loss for developing high performance CNTS solar cell, several organic and inorganic HTLs are incorporated in the Au/HTLs/CNTS/ZnS/ZnO/ITO structure. In the proposed CNTS PV device with HTLs, the thicknesses of 0.06 μm for ZnO ETL, 0.08 μm for ZnS buffer, 1.0 μm for CNTS absorber, and 0.1 μm for an HTL, respectively, have been used. Fig. 3(a) represents the J-V behaviors for the initial CNTS PV device compared to the cell configurations with various HTLs. It can be perceived that the J-V results are significantly higher in the configurations with MoO$_3$, SnS, NiO$_x$, and PEDOT.PSS HTLs than the device without HTL. Under illumination, electron-hole pairs as excess free carriers are generated and get parted by the influence of barrier potential at p-n junction. The more distant electron-hole pairs are from the p-n junction, the less effective electric field becomes to separate charge carriers. An electron reflector HTL supports effortless electron-hole separation through an additional junction like energy band bending owing to heavily doped (HTL)-low doped (absorber) arrangement in this remote region. Consequently, surface recombination mitigation at the back junction is feasible. Table 4 summarizes comparisons among device performances with different HTLs and respective CBO and VBO values for different HTLs with CNTS absorber [39,53–58].

Table 4

Outputs of CNTS-based TFSCs with various HTLs and corresponding VBO and CBO values [39,53–58].

Configurations	CBO	VBO	V_{OC} (V)	J_{SC} (mA/cm^2)	FF (%)	Efficiency (%)
MoO$_3$/CNTS/ZnS/ZnO [39,53]	1.37	0.11	1.14	9.79	78.83	8.79
SnS/CNTS/ZnS/ZnO [39,54,55]	0.07	0.20	1.13	7.52	78.67	6.68
NiO$_x$/CNTS/ZnS/ZnO [39,56–58]	2.41	0.55	1.06	7.36	76.13	5.94
PEDOT.PSS/CNTS/ZnS/ZnO [39,56]	0.97	0.51	1.11	7.38	77.16	6.30

Table 5

Lattice mismatch values for numerous HTLs with CNTS layer [43,59,66–68].

Layers	Lattice parameters			Lattice mismatch (%)
	a (Å)	b (Å)	c (Å)	
CNTS absorber [66]	5.36	5.36	5.36	–
MoO$_3$ (HTL) [59]	7.122	5.374	5.565	0.26
SnS (HTL) [43]	4.28	11.41	3.96	22.4
NiO$_x$ (HTL) [67]	8.341	–	–	43.51
PEDOT.PSS (HTL) [68]	7.7	11.7	22.5	35.83

Fig. 3(b) illustrates the band diagrams for the CNTS solar structures with various HTLs indicating VBOs and CBOs. An HTL is considered as ideal imparting large CBO and near zero VBO with the absorber which repels electron towards the bulk and pulls holes in the HTL region [51]. As revealed in Fig. 3(b) and Table 4, large positive CBO and smaller VBO values are determined for MoO$_3$ HTL. Smaller VBO at MoO$_3$/CNTS interface allows low potential barrier for more holes to ease transfer from the absorber to the rear electrode via the HTL while large CBO generates barrier for the minority electrons. Contrarily, holes are suppressed due to slightly high barriers (large VBOs) at the SnS/CNTS, NiO$_x$/CNTS, and PEDOT.PSS/CNTS interfaces, thus increasing the electron-hole recombination. Therefore, the Au/MoO$_3$/CNTS/ZnS/ZnO/ITO arrangement generates current density of 9.79 mA/cm^2 surpassing 7.52 mA/cm^2 in Au/SnS/CNTS/ZnS/ZnO/ITO, 7.36 mA/cm^2 in Au/NiO$_x$/CNTS/ZnS/ZnO/ITO, and 7.38 mA/cm^2 in Au/PEDOT. PSS/CNTS/ZnS/ZnO/ITO configurations. As recombination rate is minimized with more carriers available [42], V_{OC} is higher in the CNTS PV device with MoO$_3$ HTL along the value of 1.14 V, while configurations with SnS, NiO$_x$, and PEDOT.PSS HTLs provide V_{OC} of 1.13 V, 1.06 V, and 1.11 V respectively. The highest device outputs such as V_{OC} of 1.14 V, J_{SC} of 9.79 mA/cm^2, FF of 78.83% and efficiency of 8.79% are computed for the CNTS device with MoO$_3$ HTL as compared to that of the PV devices with other HTLs (SnS, NiO$_x$, PEDOT.PSS). In addition, the important terminology 'lattice mismatch' can be used to understand crystal perfection or imperfection of the grown material in the hetero-structure. Thus, the performance of the proposed hetero-structure can be realized by analyzing the lattice mismatch percentage. In this study, lattice mismatch δ (%), which is an interface feature defining factor, in the grown film on the substrate can be calculated using equation (4) as [43,52,64,65].

$$\delta = \frac{2|a_s - a_e|}{(a_s + a_e)} \times 100 \tag{4}$$

where a_s is the lattice constant of the substrate on which an epitaxial layer is grown and the a_e is the lattice constant of a layer. In this study, the absorber is considered to be fabricated on the HTL. Here, the lattice mismatches of MoO$_3$ HTL and other SnS, NiO$_x$, and PEDOT.PSS HTLs [42,58,66–68] with the CNTS absorber are calculated. Table 5 represents the lattice mismatch percentages between the CNTS absorber film and the various HTLs conforming to their lattice constants computed from the relation given in Eq. (4). In contrast to considerably small lattice mismatch of 0.26% calculated for the CNTS/MoO$_3$ HTL interface, large lattice mismatch values are estimated at the SnS HTL/CNTS, NiO$_x$ HTL/CNTS, and PEDOT.PSS HTL/CNTS interfaces with values of 22.4%, 43.51% and 35.83%, respectively. Consequently, it is assumed that interfacial recombination and defects at the MoO$_3$ HTL/CNTS interface are less prominent than at the interfaces between CNTS and other HTLs with high lattice mismatch values [43,65]. In this numerical study, it is revealed that through incorporation of the MoO$_3$ as an HTL at the rear side of the CNTS absorbing layer, the PV parameters of the CNTS-based heterojunction TFSCs can be significantly improved. In the subsequent parts, the simulations are carried out for the purpose of optimization of different layers and vital parameters to accomplish high performance CNTS-based TFSCs with MoO$_3$ HTL.

3.2. Influences of varying defects and thickness of absorber on PV device outputs

Inadequate film feature through fabrication results in extreme defect states governed by trap-assisted SRH recombination [69]. The diffusion length of carrier can be expressed as the mean distance that carriers pass through before recombining. When diffusion extent of charge carrier is greater than absorber thickness, the majority part of carriers can reach the respective electrodes and produce power. The trap-assisted SRH recombination model can be used to compute diffusion length where SRH recombination is characterized using the following equations (5) and (6)
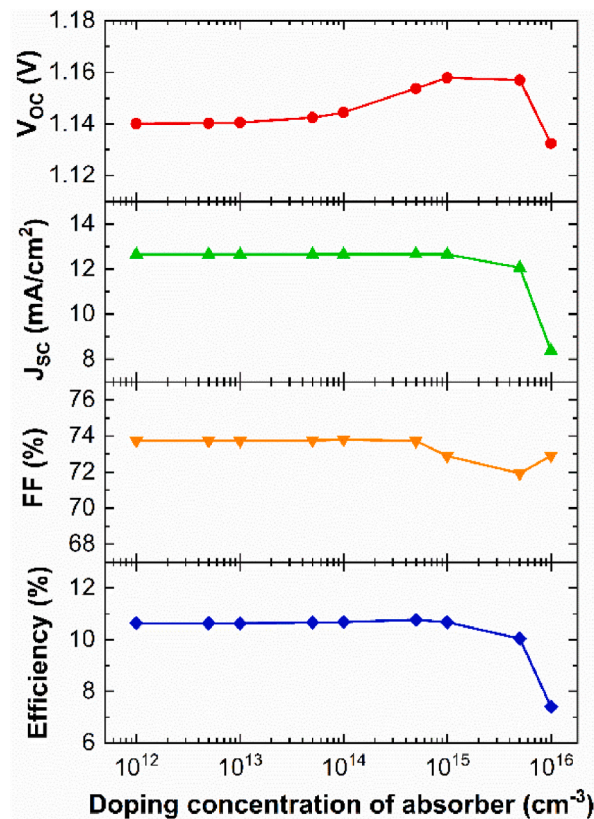
$$R_{SRH} = \frac{np - n_i^2}{\tau \left(p + n + 2n_i \cos h\left(\frac{E_i - E_t}{kT}\right)\right)} \tag{5}$$

Table 6
Variations in diffusion length (*L*) with changing defect density (N_t).

N_t (cm^{-3})	10^{17}	10^{16}	10^{15}	10^{14}
L (µm)	0.17	0.53	1.7	5.33
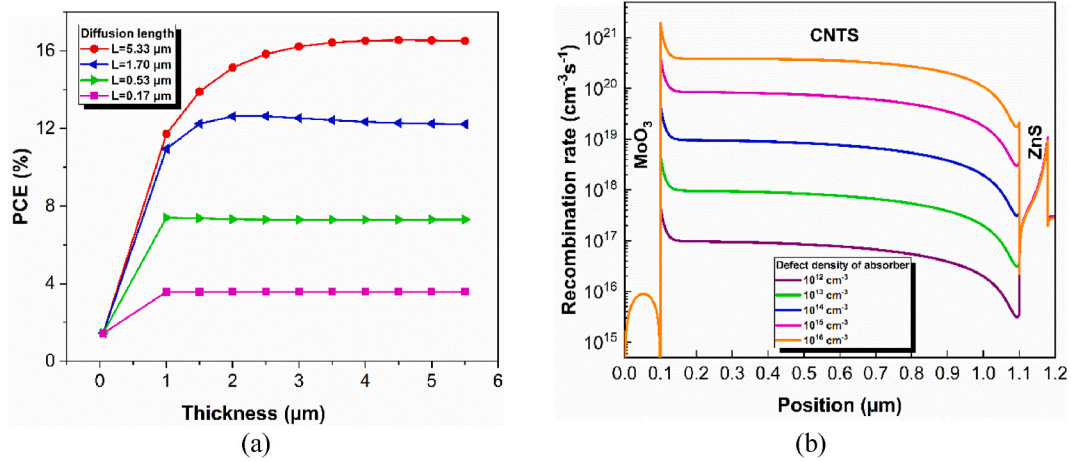
Fig. 4. (a) Variations of PCE with absorber thickness at different diffusion lengths in Au/MoO$_3$/CNTS/ZnS/ZnO/ITO configuration. (b) Recombination rate for different defect densities in CNTS absorber.

Fig. 5. Performance parameters with varying absorber doping concentration of proposed CNTS solar cell with MoO$_3$ HTL.
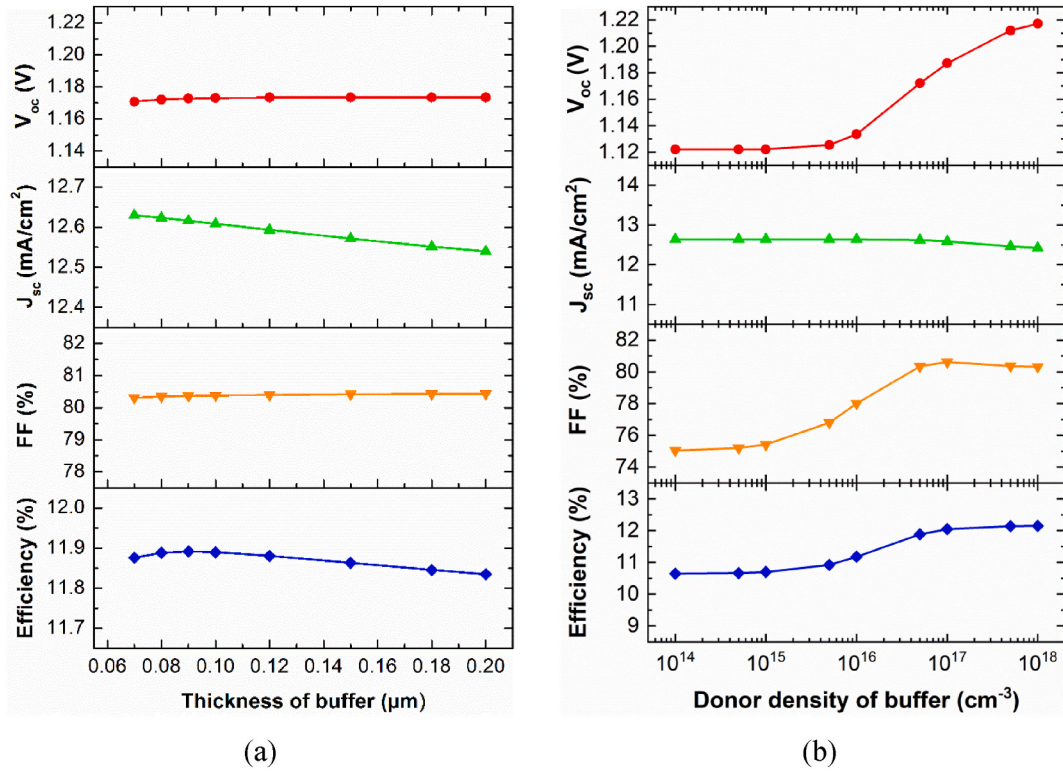
Fig. 6. Performance parameters as a function of (a) thickness and (b) doping density of ZnS buffer layer in Au/MoO₃/CNTS/ZnS/ZnO/ITO configuration.

$$\tau = \frac{1}{\sigma \times N_t \times v_{th}} \tag{6}$$

where τ is the lifetime of charge carrier and N_t and E_t are the defect concentrations and defect energy level. Capture cross-section and thermal velocity of charge carriers are represented by σ and v_{th}, respectively. The diffusion length is calculated as $L = \sqrt{D\tau}$, where diffusion coefficient $D = \frac{k_B T}{q}\mu$ with k_B representing Boltzmann's constant, T is the temperature, q is the value of electron charge, and μ is the carrier mobility. From the above equations, it can be concluded that the carrier lifetime increases with declining the defects, resulting in longer diffusion length and reduced carrier recombination [70]. Table 6 demonstrates how L in the absorber changes with N_t. Moreover, the change in PCE with the absorber thickness at various diffusion lengths is depicted in Fig. 4(a). Fig. 4(a) suggests that decreasing N_t has the same effect as the diffusion distance increment of carriers. Accordingly, the CNTS thickness can be continued to increase to the same extent as the diffusion length to achieve the high efficiency. Since, the corresponding diffusion length to N_t of 10^{15} cm⁻³ is 1.7 μm, the optimal absorber thickness of 1.0 μm is selected. Also, the recombination rate of the charge carriers in the absorber increases with expanding the defect concentrations as more defect states are created shown in Fig. 4(b). Therefore, in order to ensure the improved PV characteristics, the absorber layer should have a minimum concentration of defect centers.

3.3. Effect of absorber doping level on PV device outputs

The absorber doping and charge transport layers has a significant effect on the device efficiency. Herein, we have changed the absorber doping concentration from 10^{12} to 10^{16} cm⁻³ to study the impact of doping on the performance of the Au/MoO₃/CNTS/ZnS/ZnO/ITO device configuration, on the other hand, the thicknesses of 0.06 μm for ZnO ETL, 0.08 μm for ZnS buffer, 1.0 μm for CNTS absorber, and 0.1 μm for MoO₃ HTL, respectively, have been utilized. The simulated outputs are illustrated in Fig. 5. All the PV outputs apart from V_{OC} have almost constant up to the doping density of 10^{15} cm⁻³. An efficiency of 12.01% with V_{OC} of 1.17 V, J_{SC} of 12.73 mA/cm², and FF of 80.44% is achieved at 10^{15} cm⁻³. When acceptor density is enlarged beyond 10^{15} cm⁻³, the values of J_{SC} and conversion efficiency are decreased. The number of holes growths with enhancing the doping concentration in the p-type absorber layer, thus produces hole trap states in the absorber. These trap centers influence the mobility of the charge carriers, which leads to boost the carrier recombination at very high absorber doping concentration. Therefore, the recombination of photo-induced electrons and holes in the CNTS absorber prior on reaching the buffer/absorber and absorber/HTL interfaces at the high absorber doping density reduces the J_{SC} [52,71,72]. Furthermore, the degradation of J_{SC} is may be due to the inefficient hole transportation by the surge of impurity scattering at the high absorber doping density, thus declining the conversion efficiency. In contrast, V_{OC} is enhanced slightly
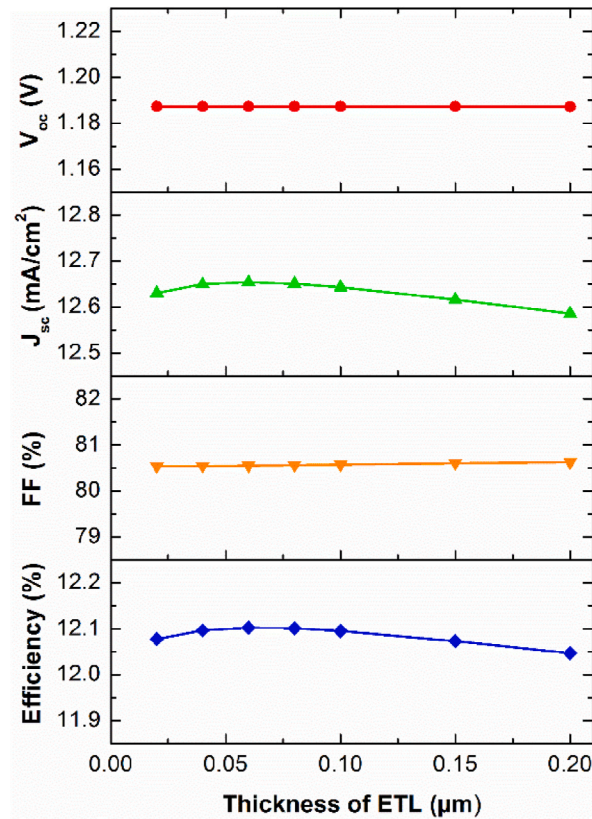
Fig. 7. PV parameters of proposed Au/MoO$_3$/CNTS/ZnS/ZnO/ITO heterojunction solar device as a function of ZnO ETL thickness.

up to the doping concentration of 5×10^{15} cm^{-3} and then is decreased. This result is may be due to larger region depleted by charge carriers with the effect of potential barrier heightened more. The reason behind this behavior is high doping density increases the amount of diffusion which in turn causes electron and hole to recombine. Hence, the moderate doping level of 10^{15} cm^{-3} with optimum 1.0 μm CNTS absorber thickness is chosen in the next simulations for further optimization of the proposed device structure.

3.4. Effects of variation in parameters of buffer and ETL on PV device outputs

The selection of buffer layer parameters is crucial to design an efficient PV cell. The key role of ZnS buffer layer is to build a junction with the absorber in the heterojunction CNTS TFSC to improve the lattice matching between the CNTS absorber and the ZnO ETL. In this segment, the optimum parameters of buffer and ETL are examined as the parameters of absorber have optimized in the previous part. Fig. 6(a)–(b) reveal the PV parameters of the proposed CNTS solar cell with MoO$_3$ HTL as a function of ZnS thickness and carrier density, respectively. To evaluate the performance variation, in this numerical analysis, the thickness from 0.07 to 0.2 μm and donor density from 10^{14} to 10^{18} cm^{-3}, respectively, are changed. It is observed in Fig. 6(a) that all the PV parameters (except J$_{SC}$ and efficiency) of the proposed CNTS TFSC are almost constant for all amounts of buffer layer thickness. Very small changes on the cell outputs for the thickness less than 0.1 μm are not significant, which is in decent concurrence with the previous work [39]. In addition, it can be seen that J$_{SC}$ is slightly declined at the thick buffer layer. It is suggested that a smaller quantity of lights may come to the absorber through the thicker buffer layer, and hence results in the insignificant current for inadequate photo-generated electrons and holes. As a result, the conversion efficiency decreases somewhat for the thick buffer layer. Therefore, a thin buffer layer should be anticipated to achieve outstanding solar cell performances. In this numerical analysis, the optimum thickness of the buffer layer is preferred to be 0.08 μm for the calculations of the solar cell output parameters. It can be also found that the PV parameters are poor at the low doping levels in the buffer but progresses as the doping concentration increases shown in Fig. 6(b). As the doping density of buffer boosts, thus generating a built-in electric field [73]. This supports acceleration in carrier transport causing higher conductivity and upgrading in the device performances. In practical, the high doping density causes reduction in the carrier mobility, and hence in this work, the doping concentration of 10^{17} cm^{-3} with the optimum 0.08 μm buffer thickness is selected. At this stage, the proposed CNTS PV device provides PCE of 12.05%, including V$_{OC}$ of 1.19 V, J$_{SC}$ of 12.59 mA/cm^2, and FF of 80.63%.

In solar cells, an ETL can be introduced for extracting and exporting the photo-induced carriers to the front electrode, reconfiguring the interface, and limiting charge recombination at front surface [74]. To absorb an ETL requires a large band gap material with high transparency so that photons can reach the absorber without parasitic absorption. The ZnO material utilized as an ETL in this work
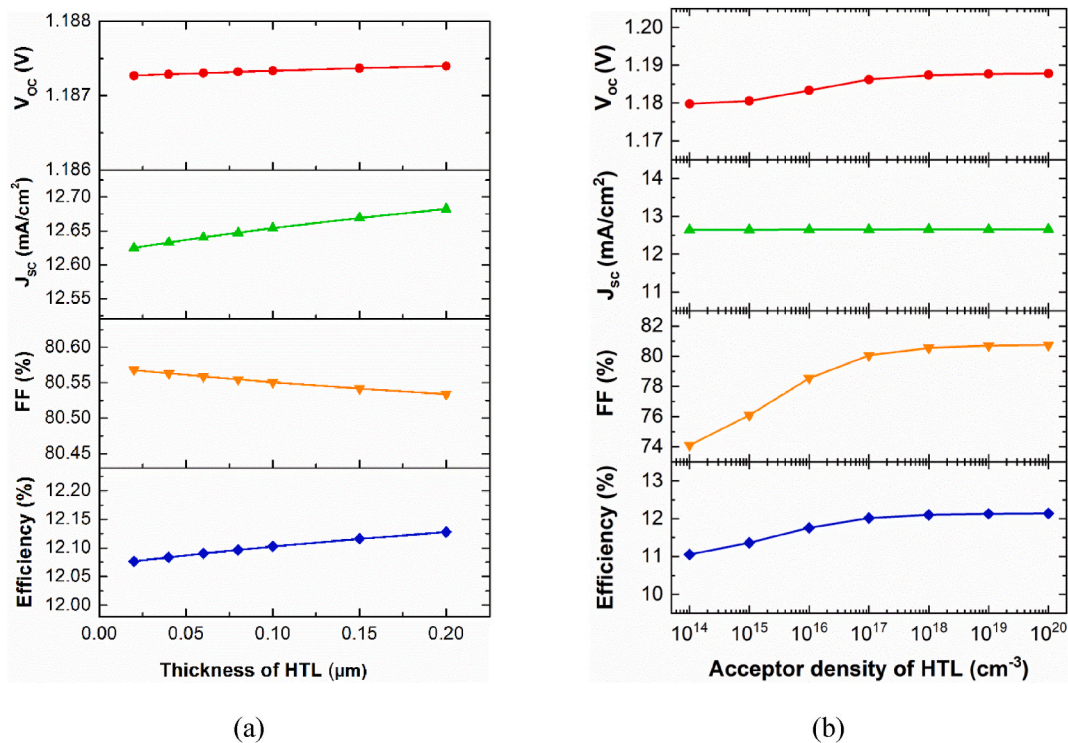
Fig. 8. Effects of (a) thickness and (b) doping density in MoO_3 HTL on outputs of CNTS TFSC.

meets both the features. Fig. 7 shows the V_{OC}, J_{SC}, FF, and efficiency versus ZnO ETL thickness. Here, the thickness is varied from 0.02 to 0.2 μm. The cell outputs excluding J_{SC} and efficiency of the offered $Au/MoO_3/CNTS/ZnS/ZnO/ITO$ heterojunction solar device are almost unchanged with the variation of ETL thickness. The value of J_{SC} is declined a little beyond the ETL thickness of 0.1 μm. This degradation of current for the thick ETL is owing to insufficient photo-generated charge carriers in the absorber, thus reducing the conversion efficiency in the solar cell. In this context, a thin ETL thickness is chosen to be 0.06 μm yielding efficiency of 12.10% including V_{OC} of 1.19 V, J_{SC} of 12.65 mA/cm^2, and FF of 80.55%.

3.5. Effects of HTL thickness and doping concentration on PV device outputs

The HTL has a significant influence on improving the outputs and stability of the PV devices [75]. This charge transport layer permits photo-induced holes to pass from the absorber layer while blocking their counterparts (electrons) to have the effect of diminished carrier recombination loss [76]. To determine the dependency of the carrier transport efficiency on the material parameters of the anticipated MoO_3 HTL, the thickness and doping concentration are changed from 0.02 to 0.2 μm and 10^{14} to 10^{20} cm^{-3}, respectively. The impacts of thickness and doping level in MoO_3 HTL on the device outputs of CNTS TFSC are illustrated in Fig. 8(a)–(b). As can be viewed from the simulated PV outputs in Fig. 8(a), all the performance parameters are somewhat changed with the variation of HTL thickness. An acute progress in electrical and optical characteristics emerges by introducing an HTL between the absorber and rear electrode. In Fig. 8(a), slight increase in J_{SC} and V_{OC} are observed with growing the HTL thickness. It can be implied that the declining rate of photo-induced carrier recombination in the effective extent of the solar cell would results in the enhancements of J_{SC} and V_{OC} with enlarging the thickness of HTL [12], thereby increasing the conversion efficiency of the PV device slightly. Also, the high energetic photons unabsorbed in the thin CNTS absorber layer may be absorbed by the MoO_3 HTL, which gives an additional advance in the device performances [42]. It can further be found that FF is somewhat decreased for further increasing the HTL thickness, this is because of the increase in resistance at back surface in the heterojunction. This behaviors in PV parameters as a function of HTL thickness have consistency with a slight variations in device outputs realized when the thickness of back surface passivation layer is varied in the range from 0.05 to 0.3 μm in the previous researches [12,43,44,77–79]. Hence, in this study, a thin HTL with thickness of 0.1 μm is selected to avoid cost and recombination as the thick HTL in the PV cell demands more materials and offers high contact resistance for carrier transmission. On the other hand, it is noticed that the PCE is enlarged from 11.05% to 12.14% for the HTL doping varied from 10^{14} to 10^{20} cm^{-3} (Fig. 8(b)). The sufficient barrier potential at the $MoO_3/CNTS$ junction may be still created even at very high HTL doping levels which prevents the minority electrons transmission towards the rear electrode from the absorber. The V_{OC} increases slightly at a high HTL doping, thus the efficiency is also enhanced moderately.

Fig. 9 represents the recombination rate at $MoO_3/CNTS$ interface for various HTL doping densities in the heterojunction $Au/MoO_3/CNTS/ZnS/ZnO/ITO$ configuration. It is found that the recombination rate at $MoO_3/CNTS$ interface declines dramatically with
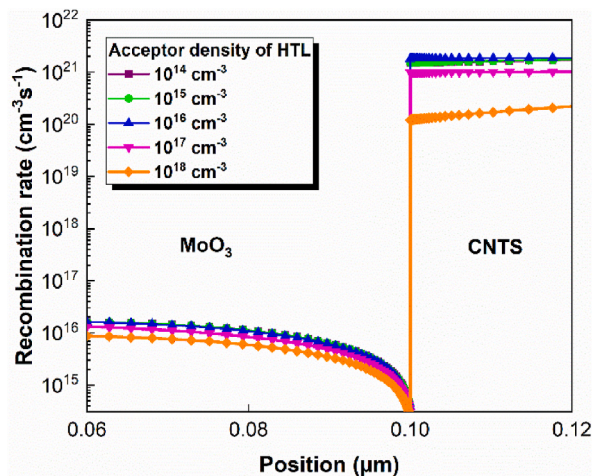
Fig. 9. Recombination rate at MoO$_3$/CNTS interface as a function of MoO$_3$ HTL carrier concentration in heterojunction configuration of Au/MoO$_3$/CNTS/ZnS/ZnO/ITO.
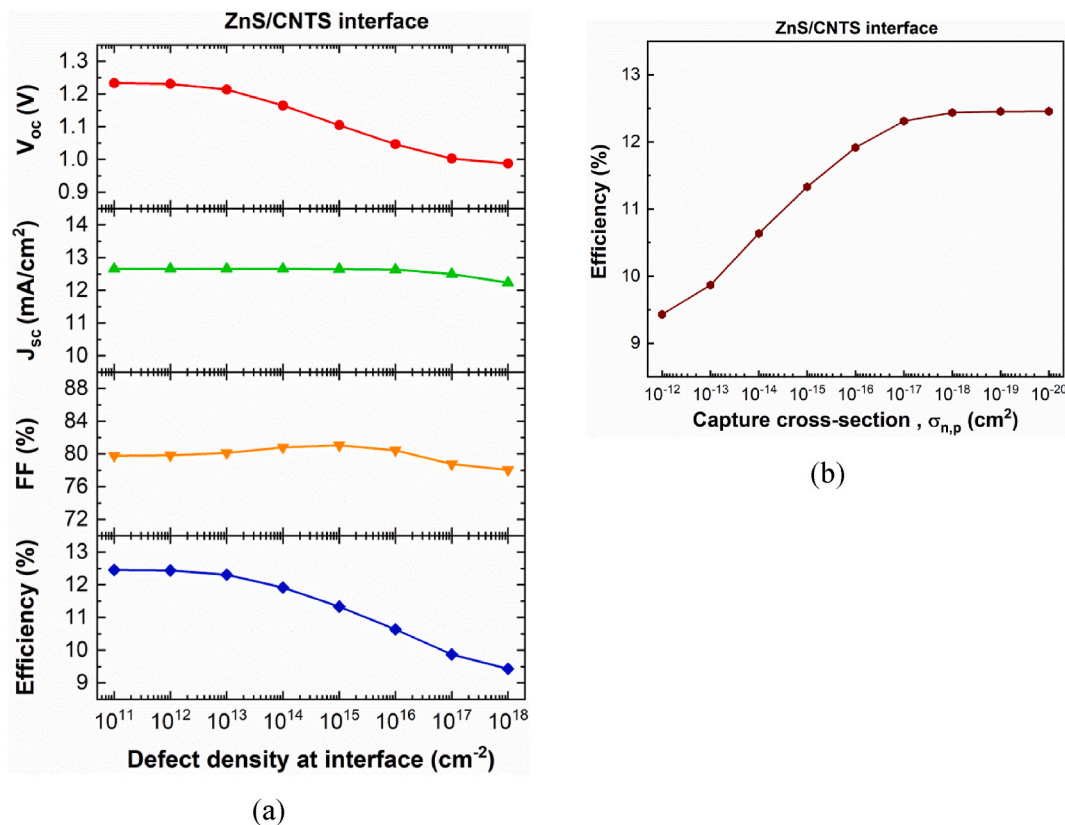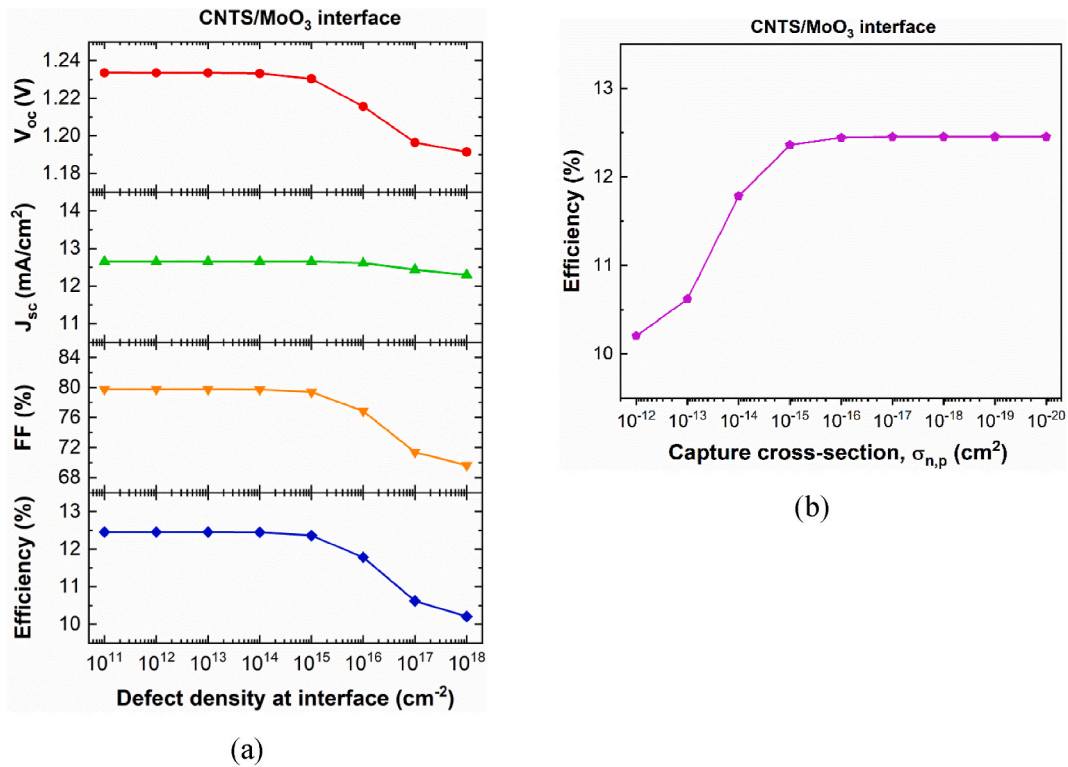

Fig. 10. (a) V$_{OC}$, J$_{SC}$, FF, and efficiency as a function of defects at CNTS/ZnS interface. (b) PCE as a function of capture cross-section of electron and hole ($\sigma_{n,p}$) at CNTS/ZnS interface.

growing the HTL acceptor density. The Fermi-level of the MoO$_3$ HTL shifted near the valence band when the doping level is increased [43]. So, there is reduction in energy barrier for the holes at the MoO$_3$/CNTS boundary resulting in minor recombination loss. At the same time, the recombination probability in the absorber also diminishes as less number of holes is available [50,80]. The MoO$_3$ HTL thickness and doping concentration are optimized at 0.1 μm and 10^{18} cm^{-3}, respectively. The PCE of 12.10% is estimated in the proposed heterojunction CNTS PV device with the layer thicknesses of 0.06 μm for ZnO, 0.08 μm for ZnS, and 1.0 μm for CNTS, correspondingly. Concurrently, the optimized values of doping concentration in ZnO, ZnS, and CNTS films are 4 × 10^{18} cm^{-3}, 10^{17}

Fig. 11. (a) PV parameters versus defect density at MoO$_3$/CNTS interface. (b) PCE as a function of capture cross-section of electron and hole ($\sigma_{n,p}$) at MoO$_3$/CNTS interface.

cm^{-3}, and 10^{15} cm^{-3}, respectively.

3.6. Effect of defect characteristics at CNTS/ZnS interface on PV device outputs

The outputs of the suggested TFSC with MoO$_3$ HTL have been comprehensively investigated for several defect properties (defect density and capture cross-section of electron and hole) associated with the CNTS/ZnS interface, as revealed in Fig. 10(a)–(b). As can be detected in Fig. 10(a), the value of J$_{SC}$ is almost invariable likely the defect state of 10^{16} cm^{-2} but V$_{OC}$ starts decreasing for the defect density beyond 10^{13} cm^{-2}. The PCE keep on the similar inclination as the V$_{OC}$ while FF decreases initially and then increases before finally dropping off. Fig. 10(b) indicates the deviation in the PCE as a function of capture cross-section of electron and hole ($\sigma_{n,p}$). The PCE is linearly growing for $\sigma_{n,p}$ value from 10^{-12} to 10^{-17} cm^2 and then is saturated. At this stage, the value of PCE is evaluated to be 12.45%. Increasing $\sigma_{n,p}$ indicates large lattice mismatch in heterojunction structure [81], and hence poor PCE is monitored at high values of $\sigma_{n,p}$. The capture cross-section and trap density both affect the carrier's lifetimes. As a result, when the capture cross-section increases, the carrier lifetime decreases due to an increase in the dimension of the trap states, which significantly lowers the performance of solar cells. According to the findings in this report, the defect at the CNTS/ZnS interface has a minor part in the performance deterioration of the CNTS-based TFSC compared to the deep level defect in the CNTS film. Defect density and $\sigma_{n,p}$ are taken as 10^{11} cm^{-2} and 10^{-19} cm^2, respectively, at the CNTS/ZnS interface for following simulations.

3.7. Effect of defect properties at MoO$_3$/CNTS interface on PV device outputs

In the present study, the impacts of defect characteristics like defect states and trap capture cross-section ($\sigma_{n,p}$) at the MoO$_3$/CNTS interface on the device outputs are also examined and the simulated outputs are as illustrated in Fig. 11(a) to 11(b). The defect density and $\sigma_{n,p}$ are varied from 10^{11} to 10^{18} cm^{-2} and 10^{-12} to 10^{-20} cm^2, respectively. In Fig. 11(a), no significant change in performance parameters till the defect state of 10^{14} cm^{-2} is observed. When the defects exceed 10^{14} cm^{-2}, the device performances slightly degrade as V$_{OC}$ from 1.23 to 1.19 V, J$_{SC}$ from 12.65 to 12.29 mA/cm^2, FF from 79.74% to 69.64%, and efficiency from 12.45% to 10.20%. Also, in Fig. 11(b), increments in capture cross-section of electron and hole ($\sigma_{n,p}$) cause deterioration of the MoO$_3$/CNTS interface quality and for this reason, the PCE is in descending approach. As found in this section and in the previous reports [82,83], the interface defect density properties close to the back interface (MoO$_3$/CNTS) have a trivial effect on the cell performances when compared to the front (illuminated side) interface (CNTS/ZnS). At optimized values of defect concentration to 10^{11} cm^{-2} and $\sigma_{n,p}$ to 10^{-19} cm^2, the PCE of 12.46% is obtained for the proposed heterojunction CNTS solar cell.
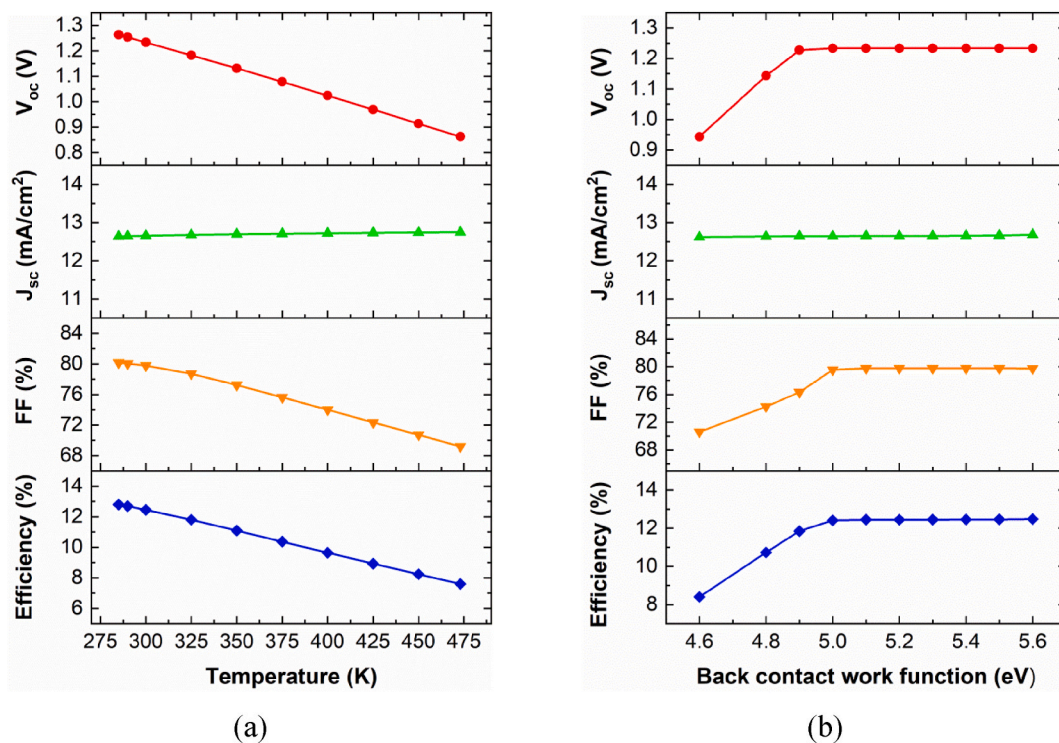
Fig. 12. Impacts of (a) operating temperature and (b) back electrode work function on V_{oc}, J_{sc}, FF, and PCE of proposed CNTS-based solar cell with MoO$_3$ HTL.

3.8. Impacts of operative temperature and work function on PV device outputs

Ambient temperature variation has a sensitive effect on the solar cells. Temperature increment reduces the band gap of the semiconductor, affecting most of the parameters of the solar cell [52]. To analyze the steadiness of the anticipated CNTS PV device with MoO$_3$ HTL, the effective temperature is varied from 285 to 473 K and the deviation of the PV parameters including V_{oc}, J_{sc}, FF, and PCE are displayed in Fig. 12(a). The V_{oc} in a solar cell is the most affected parameter by temperature enhancement as the reverse saturation current rises [49]. V_{oc} declines from 1.26 to 0.86 V estimated at the temperature ranged from 285 to 473 K, respectively. The J_{SC} boosts slightly with increasing the temperature as extra photons have enough energy for creating electron-hole pair due to reduced bandgap but the effect is small manifested in Fig. 12(a). The recombination procedure of the electron-hole pair amid the conduction band and the valence band is augmented. As a result, the reverse saturation current will be increased with expanding the operating temperature [42,52]. The energy bandgap of semiconductors in the solar cell minimizes at the high temperature, consequently small increase in the J_{SC}. This outcome would lead to drop in the V_{OC}. Therefore, the linear diminution in the V_{oc} and the slight rise in the J_{sc} promote to the reduction in the FF and the conversion efficiency of the PV cell at the high temperature [84]. Similar results on the temperature dependence of solar cell performances have been found in the previously published research works [42,43,52,84–86]. The PCE and FF of the designed CNTS solar cell fall from 12.80% to 7.61% and 80.16%–69.18%, respectively, when the temperature is altered from 285 to 473 K.

High evaporation temperature and expensive equipment are necessary to utilize the gold (Au) material presented in the previous sections as a back electrode for a PV cell. Thus, the cost of the metal contact as well as the total expense of the solar device will be increased [87]. As shown in Fig. 12(b), the influence of the work function of different back electrode metals on the outputs of the designed device structure is studied. The high Schottky barrier formed at the absorber/back contact may hinder the hole transfer and reduces the overall device outcomes. The PV characteristics rise considerably with increasing the work function of back side electrode as the Schottky barrier decreases [44]. Since an Ohmic-contact is formed instead of the Schottky-contact at the rear electrode of the heterojunction device structure with increasing the work function, subsequently confirming an easier moving of holes from the absorber layer. In this context, the recombination loss in the TFSC may be insignificant, as a result the PCE is enhanced remarkably. It can also be seen in Fig. 12(b) that all the outputs of the proposed CNTS device with MoO$_3$ HTL are saturated for the work function larger than 5.0 eV. To recognize an efficient CNTS solar device, it can be suggested on the basis of these findings that the back side electrode with work function higher than 5.0 eV is obligatory. In the present work, the Ni metal has been selected for the back electrode by considering the economical and stability [88,89].
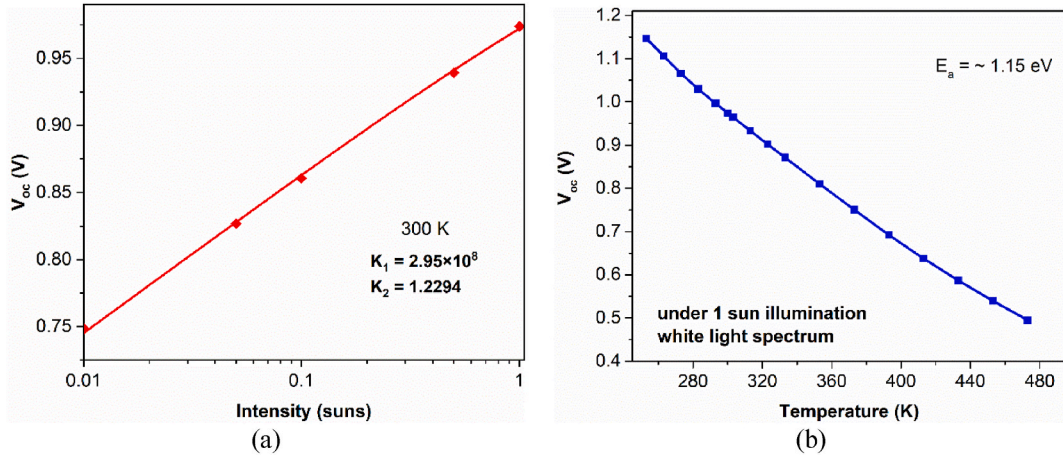
Fig. 13. Variations of (a) V_{oc} on light intensity and (b) temperature at one Sun illumination.

3.9. Recombination coefficients analysis

The process of recombination at the intersection of the various layers has a significant impact on the voltage (V_{OC}) in CNTS TFSCs. Voltage deficit is still the main reason TFSCs work poorly. Calculating the various recombination rates is essential to reducing the amount of recombination that takes place within the various PV device components and lowering the voltage shortage of the device. When the circuit is open, the carriers in the device rejoin. Understanding the recombination processes can therefore be aided by measuring V_{OC} under varied temperature and light illumination circumstances. Utilizing certain mathematical speculations and SRH recombination characteristics, the quantitatively determined recombination amounts at the CNTS/ZnS junction ($R^{i,f}$), quasi-neutral area (R^b), rear contact/CNTS ($R^{i,b}$), and depletion locale (R^d) have been computed for the device architecture shown in Fig. 1(b). The relationships in equation (7), which have been established by earlier studies, demonstrate how temperature and voltage affect these constants [90–92].

$$R^{i,f} = R_0^{i,f} e^{\frac{qV}{k_B T}}$$

$$R^d = R_0^d e^{\frac{qV}{2k_B T}}$$

$$R^b = R_0^b e^{\frac{qV}{k_B T}}$$

$$R^{i,b} = R_0^{i,b} e^{\frac{qV}{k_B T}}$$

(7)

where k_B is the Boltzmann value, $R_0^{i,f}, R_0^d, R_0^b$, and $R_0^{i,b}$ are bias-independent recombination coefficients at various regions mentioned above. At V_{OC}, the entire carrier creation throughout the absorber layer is derived by correlating the result to the net recombination.

$$\left(R_0^{i,f} + R_0^b + R_0^{i,b}\right) e^{\frac{qV_{oc}}{k_B T}} + R_0^d e^{\frac{qV_{oc}}{2k_B T}} - G_a W = 0$$

(8)

after the aforementioned equation (8) is solved, we may write

$$V_{oc} = \frac{2k_B T}{q} \ln\left[\frac{1}{2} \frac{R_0^d}{\left(R_0^{i,f} + R_0^b + R_0^{i,b}\right)} \left(\sqrt{4 G_a W \frac{\left(R_0^{i,f} + R_0^b + R_0^{i,b}\right)}{\left(R_0^d\right)^2} + 1} - 1\right)\right]$$

(9)

Equation (9) can be further expressed as

$$V_{oc} = \frac{2k_B T}{q} \ln\left[K_1\left(\sqrt{G_a K_2 + 1} - 1\right)\right]$$

(10)

where

$$K_1 = \frac{1}{2} \frac{R_0^d}{\left(R_0^{i,f} + R_0^b + R_0^{i,b}\right)}$$

Table 7

Extracted K_1 and K_2, and recombination coefficients of proposed CNTS solar cell.

K_1	K_2 (suns^{-1})	R_0^i (cm^{-2}S^{-1})	R_0^b (cm^{-2}S^{-1})	R_0^d (cm^{-2}S^{-1})	R^i (cm^{-2}S^{-1})	R^b (cm^{-2}S^{-1})	R^d (cm^{-2}S^{-1})
2.95×10^8	1.2294	18	18	3.88×10^6	2.47×10^9	2.47×10^9	5.36×10^{14}

Table 8

Optimized physical parameters for Ni/MoO$_3$/CNTS/ZnS/ZnO/ITO cell configuration.

Optimized parameters (unit)	n$^+$-type ETL (ZnO)	n-type Buffer (ZnS)	p-type Absorber (CNTS)	p$^+$-type HTL (MoO$_3$)	Interface defect density	
					CNTS/ZnS	MoO$_3$/CNTS
W (μm)	0.06	0.08	1.0	0.1		
N_D (cm^{-3})	4×10^{18}	10^{17}	–	–		
N_A (cm^{-3})	–	–	10^{15}	10^{18}		
N_t (cm^{-3})	10^{16}	10^{16}	10^{15}	10^{15}		
$\sigma_{n,p}$ (cm^2)					10^{-19}	10^{-19}
Total density (cm^{-2})					10^{11}	10^{11}

Table 9

Comparison of PV parameters among different CNTS solar cell configurations.

Device architectures		V_{OC} (V)	J_{SC} (mA/cm^2)	FF (%)	PCE (%)
Initial	Au/CNTS/ZnS/ZnO/ITO (Experimental) [27]	0.75	6.82	53.10	2.71
	Au/CNTS/ZnS/ZnO/ITO (Simulation) [this work]	0.75	6.98	51.16	2.71
With HTL	Au/MoO$_3$/CNTS/ZnS/ZnO/ITO	1.13	9.62	78.05	8.79
Final optimization	Ni/MoO$_3$/CNTS/ZnS/ZnO/ITO	1.23	12.66	79.78	12.46
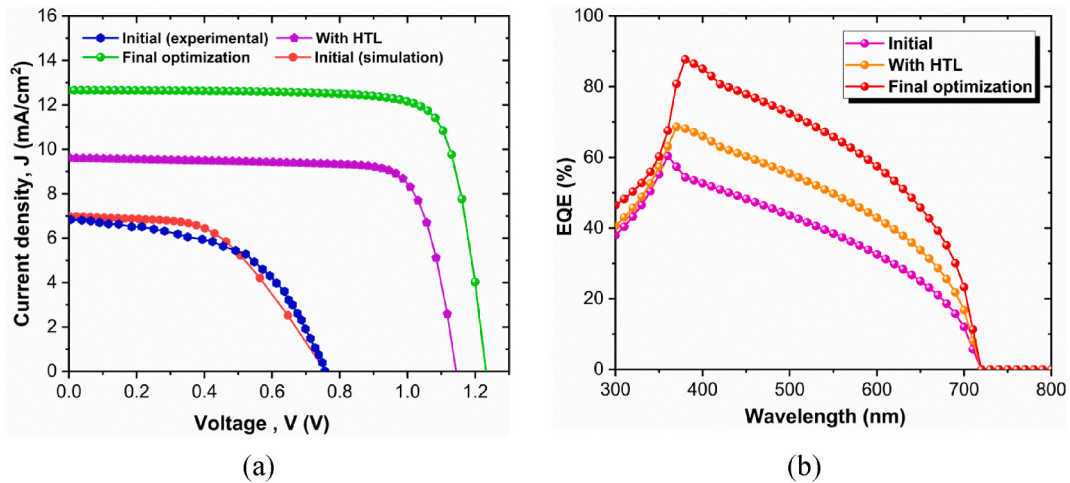
Fig. 14. (a) J-V characteristics and (b) EQE for several CNTS solar cells.

$$K_2 = \frac{4W\left(R_0^{i,f} + R_0^b + R_0^{i,b}\right)}{\left(R_0^d\right)^2}$$

It is obvious from equation (10) that voltage is a linear consequence of temperature (T) and excitation light intensity (G$_a$). As shown in Fig. 13(a)–(b), we have simulated the CNTS TFSC in two distinct conditions: (1) variable illuminations with a 300 K constant temperature, and (2) changing temperature with a stable lighting of 1 sun. Then, we have used equations (9) and (10) to fit the curve in Fig. 13(a) in order to calculate the K_1 and K_2 values for the device provided in Table 7. Lastly, we computed the values of R^i, R^d, and R^b at the CNTS/ZnS, depletion, and quasi-neutral regions, respectively, using Fig. 13(b) and the linked formulas from the prior research [90]. Table 7 also includes the $R_0^{i,f}, R_0^b,$ and R_0^d values.

3.10. Overall performances of optimized CNTS-based PV devices

Following a comprehensive research of the effect of various aspects of the solar cell on the outputs, a simulation for the optimized device is performed. The physical parameters optimized for high performance heterojunction Ni/MoO$_3$/CNTS/ZnS/ZnO/ITO device are listed in Table 8. In addition, a comparison of the PV parameters among different CNTS solar cell configurations is summarized in Table 9. The J-V curves and external quantum efficiency (EQE) among the different heterojunction CNTS TFSCs are demonstrated in Fig. 14(a)–(b), respectively. Utilizing the Ni as a back contact in the proposed CNTS TFSC, it is noted that efficiency of 12.46% including V$_{OC}$ of 1.23 V, J$_{SC}$ of 12.66 mA/cm^2, and FF of 79.78% is evaluated for the optimized device. It can be concluded that incorporation of an appropriate HTL in the CNTS solar structure numerically modeled according to experimentally extracted parameters and then optimization of these parameters can improve the overall device performances to establish new research opportunities for the CNTS materials in the PV applications.

4. Conclusions

This paper reports the predictive simulation model of the CNTS-based TFSC with MoO$_3$ as HTL is developed by the SCAPS-1D software in order to better comprehend a rear surface passivation. It is noticed that the low experimental PCE finds its root in unoptimized band alignment at the back metal electrode/CNTS absorber interface. Consequently, the PV outputs optimization is taken up by concentrating on appropriate choice of the HTL. We have demonstrated comparison of performance parameters incorporating several HTL materials in the CNTS-based cell. These simulation results reveal that the band alignment with high CBO and low VBO values at the rear electrode is essentially required to enhance the cell performances. Herein, it is uncovered that incorporating the MoO$_3$ as HTL at the rear side of the CNTS absorber successfully boosts the PV characteristics among other back surface passivation layers. With this modification, the efficiency is obtained to be 8.79% from a previous efficiency of 2.71%. Further optimization of the suggested PV cell is conducted by examining the effects of thickness, carrier density, bulk, and interface defects of respective layers. We have also examined the cell's outputs of the developed solar configuration by altering operative temperature and work function of back side electrode. The optimum thickness and doping concentration are preferred to be 0.06 μm and 4×10^{18} cm^{-3}, 0.08 μm and 10^{17} cm^{-3}, 1.0 μm and 10^{15} cm^{-3}, 0.1 μm and 10^{18} cm^{-3} for the ZnO ETL, ZnS buffer, CNTS absorber, and MoO$_3$ HTL, respectively. By utilizing all the optimized parameters, the PV outputs such as V$_{oc}$ of 1.23 V, J$_{SC}$ of 12.66 mA/cm^2, FF of 79.78% and efficiency of 12.46% are calculated. These outcomes imply that the MoO$_3$ can be utilized as a promising HTL in the CNTS-based TFSC. Hence, this investigation will be helpful for researchers to develop an inexpensive and highly efficient CNTS-based PV device.

Data availability statement

Data will be made available on request.

CRediT authorship contribution statement

Most Marzia Khatun: Conceptualization, Investigation, Methodology, Software, Validation, Writing – original draft. **Adnan Hosen:** Formal analysis, Investigation, Software, Validation. **Sheikh Rashel Al Ahmed:** Conceptualization, Investigation, Supervision, Validation, Writing – review & editing.

Declaration of competing interest

The authors declare that they have no known competing financial interests or personal relationships that could have appeared to influence the work reported in this paper.

Acknowledgement

References

[1] A. Goetzberger, J. Luther, G. Willeke, Solar cells: past, present, future, Sol. Energy Mater. Sol. Cells 74 (2002) 1–11.
[2] J.S. Liu, C.-H. Kuan, S.-C. Cha, W.-L. Chuang, G.J. Gau, J.-Y. Jeng, Photovoltaic technology development: a perspective from patent growth analysis, Sol. Energy Mater. Sol. Cells 95 (2011) 3130–3136.
[3] N. Espinosa, Y.S. Zimmermann, G.A.D. Benatto, M. Lenz, F.C. Krebs, Outdoor fate and environmental impact of polymer solar cells through leaching and emission to rainwater and soil, Energy Environ. Sci. 9 (2016) 1674–1680.
[4] E. Płaczek-Popko, Top PV market solar cells 2016, Opto-electron, Rev. E. 25 (2017) 55–64.
[5] M.A. Green, Silicon Solar Cells: Evolution, High-Efficiency Design and Efficiency Enhancements, Semicond. Sci. Technol. 8, 1993, pp. 1–12.
[6] T. Saga, Advances in crystalline silicon solar cell technology for industrial mass production, NPG Asia Mater. 2 (2010) 96–102.
[7] M. Xu, T. Bearda, H.S. Radhakrishnan, S.K. Jonnak, M. Hasan, S. Malik, M. Filipic, V. Depauw, K. Van Nieuwenhuysen, Y. Abdulraheem, M. Debucquoy, I. Gordon, J. Szlufcik, J. Poortmans, Silicon heterojunction interdigitated back contact solar cells bonded to glass with efficiency>21, Sol. Energy Mater. Sol. Cells 165 (2017) 82–87.

[8] M.A. Green, Thin-film solar cells: review of materials, technologies and commercial status, J. Mater. Sci. Mater. Electron. 18 (S1) (2007) 15–19.

[9] M. Powalla, S. Paetel, E. Ahlswede, R. Wuerz, C.D. Wessendorf, T.M. Friedlmeier, Thin-film solar cell exceeding 22% solar cell efficiency: an overview on CdTe-, Cu(In, Ga)Se$_2$-, and perovskite-based materials, Appl. Phys. Rev. 5 (2018), 041602.

[10] A. Hu, J. Zhou, P. Zhong, X. Qin, M. Zhang, Y. Jiang, X. Wu, D. Yang, High-efficiency CdTe-based thin-film solar cells with unltrathin CdS:O window layer and processes with post annealing, Sol. Energy 214 (2021) 319–325.

[11] K. Vijayan, S.P. Vijayachamundeeswari, K. Sivaperuman, N. Ahsan, T. Logu, Y. Okada, A review on advancements, challenges, and prospective of copper and non-copper based thin-film solar cells using facile spray pyrolysis technique, Sol. Energy 234 (2022) 81–102.

[12] A. Isha, A. Kowsar, A. Kuddus, M.K. Hossain, M.H. Ali, M.D. Haque, M.F. Rahman, High efficiency Cu$_2$MnSnS$_4$ thin film solar cells with SnS BSF and CdS ETL layers: a numerical simulation, Heliyon 9 (2023), e15716.

[13] A.G. Aberle, Thin-film solar cells, Thin Solid Films 517 (2009) 4706–4710.

[14] T.D. Lee, A.U. Ebong, A review of thin film solar cell technologies and challenges, Renew. Sustain. Energy Rev. 70 (2017) 1286–1297.

[15] S. Sundaram, K. Shanks, H. Upadhyaya, Thin Film Photovoltaics-A Comprehensive Guide to Solar Energy Systems, Academic Press, 2018, pp. 361–370.

[16] Y. Cui, R. Deng, G. Wang, D. Pan, A general strategy for synthesis of quaternary semiconductor Cu$_2$MSnS$_4$ (M = Co^{2+}, Fe^{2+}, Ni^{2+}, Mn^{2+}) nanocrystals, J. Mater. Chem. 22 (2012) 23136–23140.

[17] T.-X. Wang, Y.-G. Li, H.-R. Liu, H. Li, S.-X. Chen, Flower-like Cu$_2$NiSnS$_4$ nanoparticles synthesized by a facile solvothermal method, Mater. Lett. 124 (2014) 148–150.

[18] C. Yang, Y. Chen, M. Lin, S. Wu, L. Li, W. Liu, X. Wu, F. Zhang, Structural, optical and magnetic properties of Cu$_2$NiSnS$_4$ thin films deposited by facile one-step electrodeposition, Mater. Lett. 166 (2016) 101–104.

[19] M.S. Kumar, S.P. Madhusudanan, S.K. Batabyal, Substitution of Zn in earth abundant Cu$_2$ZnSn(S,Se)$_4$ based thin film solar cells—a status review, Sol. Energy Mater. Sol. Cells 185 (2018) 287–299.

[20] D.E. Carlson, C.R. Wronski, Amorphous silicon solar cell, Appl. Phys. Lett. 28 (1976) 671–673.

[21] J. Major, R. Treharne, L. Phillips, K. Durose, A low-cost nontoxic post-growth activation step for CdTe solar cells, Nature 511 (2014) 334–337.

[22] W.K. Metzger, I.L. Repins, M. Contreras, Long lifetimes in high-efficiency Cu(In,Ga)Se$_2$ solar cells, Appl, Phys. Lett. 93 (2008), 022110.

[23] P. Jackson, D. Hariskos, E. Lotter, S. Paetel, R. Wuerz, R. Menner, W. Wischmann, M. Powalla, New world record efficiency for Cu(In,Ga)Se$_2$ thin-film solar cells beyond 20, Prog. Photovolt 19 (2011) 894–897.

[24] A. Kamble, K. Mokurala, A. Gupta, S. Mallick, P. Bhargava, Synthesis of Cu$_2$NiSnS$_4$ nanoparticles by hot injection method for photovoltaic applications, Mater. Lett. 137 (2014) 440–443.

[25] F. Ozel, E. Aslan, B. Istanbullu, O. Akay, I. Hatay Patir, Photocatalytic hydrogen evolution based on Cu$_2$ZnSnS$_4$, Cu$_2$NiSnS$_4$ and Cu$_2$CoSnS$_4$ nanocrystals, Appl. Catal. B Environ. 198 (2016) 67–73.

[26] H.-J. Chen, S.-W. Fu, T.-C. Tsai, C.-F. Shih, Quaternary Cu$_2$NiSnS$_4$ thin films as a solar material prepared through electrodeposition, Mater. Lett. 166 (2016) 215–218.

[27] A. Ghosh, D.K. Chaudhary, A. Biswas, R. Thangavel, G. Udayabhanu, Solution-processed Cu$_2$XSnS$_4$ (X = Fe, Co, Ni) photo-electrochemical and thin film solar cells on vertically grown ZnO nanorod arrays, RSC Adv. 6 (2016) 115204–115212.

[28] K. Mokurala, S. Mallick, P. Bhargava, S. Siol, T.R. Klein, M.F.A.M. van Hest, Influence of dipping cycles on physical, optical, and electrical properties of Cu$_2$NiSnS$_4$: direct solution dip coating for photovoltaic applications, J. Alloys Compd. 725 (2017) 510–518.

[29] G.S.D. Babu, X.S. Shajan, S. Alwin, V. Ramasubbu, G.M. Balerao, Effect of reaction period on stoichiometry, phase purity, and morphology of hydrothermally synthesized Cu$_2$NiSnS$_4$ Nanopowder, J. Electron. Mater. 47 (2018) 312–322.

[30] M.M.S. Sanad, A.M. Elseman, M.M. Elsenety, M.M. Rashad, B.A. Elsayed, Facile synthesis of sulfide-based chalcogenide as hole-transporting materials for cost-effective efficient perovskite solar cells, J. Mater. Sci. Mater. Electron. 30 (2019) 6868–6875.

[31] S. Dridi, N. Bitri, M. Abaab, Synthesis of quaternary Cu$_2$NiSnS$_4$ thin films as a solar energy material prepared through «spray» technique, Mater. Lett. 204 (2017) 61–64.

[32] C.L. Yang, Y.H. Chen, M. Lin, S.L. Wu, L. Li, W.C. Liu, X.S. Wu, F.M. Zhang, Structural, optical and magnetic properties of Cu$_2$NiSnS$_4$ thin films deposited by facile one-step electrodeposition, Mater. Lett. 166 (2016) 101–104.

[33] J. Mani, S. Radha, A.S. Alagar Nedunchezhian, R. Rajkumar, C.K. Amaljith, M. Arivanandhan, R. Jayavel, G. Anbalagan, A facile synthesis of hierarchical Cu$_2$NiSnS$_4$ nanostructures with low thermal conductivity for thermoelectric applications, J. Solid State Chem. 310 (2022), 123088.

[34] D. Ait elhaj, A. El kissani, M. Elyaagoubi, H. Ait dads, F. Welatta, L. Nkhaili, H. Chaib, A. Outzourhit, Development of Cu$_2$NiSnS$_4$ based thin film solar cells without a sulfurization step, Mater. Sci. Semicond. Process. 107 (2020) 104811.

[35] S. Rondiya, N. Wadnerkar, Y. Jadhav, S. Jadkar, S. Haram, M. Kabir, Structural, electronic, and optical properties of Cu$_2$NiSnS$_4$: a combined experimental and theoretical study toward photovoltaic applications, Chem. Mater. 29 (2017) 3133–3142.

[36] Sn Li, Rx Ma, Jw Niu, Synthesis and opto-electrical properties of Cu$_2$NiSnS$_4$ nanoparticles using a facile solid-phase process at low temperature, Optoelectron. Lett. 16 (2020) 401–404.

[37] H.I. Elsaeedy, Growth, structure, optical and optoelectrical characterizations of the Cu$_2$NiSnS$_4$ thin films synthesized by spray pyrolysis technique, J. Mater. Sci. Mater. Electron. 30 (2019) 12545–12554.

[38] S. Rühle, Tabulated values of the Shockley–Queisser limit for single junction solar cells, Sol. Energy 130 (2016) 139–147.

[39] Y.H. Khattak, F. Baig, S. Ullah, B. Mari, S. Beg, K. Khan, Effect of Cu$_2$O hole transport layer and improved minority carrier life time on the efficiency enhancement of Cu$_2$NiSnS$_4$ based experimental solar cell, J. Renew. Sustain. Energy 10 (2018) 043502.

[40] Y.H. Khattak, F. Baig, B.M. Soucase, S. Beg, S.R. Gillani, S. Ahmed, Efficiency enhancement of novel CNTS/ZnS/Zn (O,S) thin film solar cell, Optik 171 (2018) 453–462.

[41] Y. Cao, X. Zhu, H. Chen, X. Zhang, J. Zhou, Z. Hu, J. Pang, Towards high efficiency inverted Sb$_2$Se$_3$ thin film solar cells, Sol. Energy Mater. Sol. Cells 200 (2019), 109945.

[42] S.R.A. Ahmed, A. Sunny, S. Rahman, Performance enhancement of Sb$_2$Se$_3$ solar cell using a back surface field layer: a numerical simulation approach, Sol. Energy Mater. Sol. Cells 221 (2021), 110919.

[43] M.A. Rahman, Enhancing the photovoltaic performance of Cd-free Cu$_2$ZnSnS$_4$ heterojunction solar cells using SnS HTL and TiO$_2$ ETL, Sol. Energy 215 (2021) 64–76.

[44] A. Hosen, S.R.A. Ahmed, Performance analysis of SnS solar cell with a hole transport layer based on experimentally extracted device parameters, J. Alloys Compd. 909 (2022), 164823.

[45] L. Zhang, C. Jiang, C. Wu, H. Ju, G. Jiang, W. Liu, C. Zhu, T. Chen, V$_2$O$_5$ as hole transporting material for efficient all inorganic Sb$_2$S$_3$ solar cells, ACS Appl. Mater. Interfaces 10 (2018) 27098–27105.

[46] K. Li, S. Wang, C. Chen, R. Kondrotas, M. Hu, S. Lu, C. Wang, W. Chen, J. Tang, 7.5% n-i-p Sb$_2$Se$_3$ solar cells with CuSCN as hole-transport layer, J. Mater. Chem. A 7 (2019) 9665–9672.

[47] I.E. Tinedert, A. Saadoune, I. Bouchama, M.A. Saeed, Numerical modelling and optimization of CdS/CdTe solar cell with incorporation of Cu$_2$O HT-EBL layer, Opt. Mater. 106 (2020), 109970.

[48] Y. Xiao, H. Wang, H. Kuang, Numerical simulation and performance optimization of Sb$_2$S$_3$ solar cell with a hole transport layer, Opt. Mater. 108 (2020), 110414.

[49] A. Sunny, S.R.A. Ahmed, Numerical simulation and performance evaluation of highly efficient Sb$_2$Se$_3$ solar cell with tin sulfide as hole transport layer, Phys. Stat. Sol.(b) 258 (2021), 2000630.

[50] M.M. Khatun, A. Sunny, S.R.A. Ahmed, Numerical investigation on performance improvement of WS$_2$ thin-film solar cell with copper iodide as hole transport layer, Sol. Energy 224 (2021) 956–965.

[51] D. Ompong, J. Singh, High open-circuit voltage in perovskite solar cells: the role of hole transport layer, Org. Electron. 63 (2018) 104–108.

[52] S. Rahman, S.R.A. Ahmed, Photovoltaic performance enhancement in CdTe thin-film heterojunction solar cell with Sb_2S_3 as hole transport layer, Sol. Energy 230 (2021) 605–617.

[53] W. Li, W. Li, Y. Feng, C. Yang, Numerical analysis of the back interface for high efficiency wide band gap chalcopyrite solar cells, Sol. Energy 180 (2019) 207–215.

[54] G.H. Yue, L.S. Wang, X. Wang, Y.Z. Chen, D.L. Peng, Characterization and optical properties of the single crystalline SnS nanowire arrays, Nanoscale Res. Lett. 4 (2009) 359–363.

[55] S. Kabouche, Y. Louafi, B. Bellal, M. Trari, Electrochemical growth of SnS thin film: application to the photocatalytic degradation of rhodamine B under visible light, Appl. Phys. A 123 (2017) 545.

[56] F. Azri, A. Meftah, N. Sengouga, A. Meftah, Electron and hole transport layers optimization by numerical simulation of a perovskite solar cell, Sol. Energy 181 (2019) 372–378.

[57] M.S. Shamna, K.S. Nithya, K.S. Sudheer, Simulation and optimization of $CH_3NH_3SnI_3$ based inverted perovskite solar cell with NiO as Hole transport material, Mater. Today: Proc. 33 (2020) 1246–1251.

[58] K.D. Jayan, V. Sebastian, Comprehensive device modelling and performance analysis of $MASnI_3$ based perovskite solar cells with diverse ETM, HTM and back metal contacts, Sol. Energy 217 (2021) 40–48.

[59] C. Julien, B. Yebka, Electrochemical features of lithium batteries based on molybdenum-oxide compounds, in: C. Julien, Z. Stoynov (Eds.), Materials for Lithium-Ion Batteries, NATO Science Series, vol. 85, Springer, Dordrecht, 2000, pp. 263–273.

[60] M. Burgelman, K. Decock, A. Niemegeers, J. Verschraegen, S. Degrave, SCAPS Manual (Version: 3.3.07, Department of Electronics and Information Systems, University of Gent, Belgium, 2023. https://scaps.elis.ugent.be (accessed: March.

[61] M. Burgelman, P. Nollet, S. Degrave, Modelling polycrystalline semiconductor solar cells, Thin Solid Films 361–362 (2000) 527–532.

[62] M. Gloeckler, J.R. Sites, Efficiency limitations for wide-band-gap chalcopyrite solar cells, Thin Solid Films 480 (2005) 241–245.

[63] M.S. Islam, S. Rahman, A. Sunny, M.A. Haque, M.S. Mian, S.R.A. Ahmed, Numerical study of highly efficient tin-based perovskite solar cell with MoS_2 hole transport layer, Z. Naturforsch. 76 (2021) 1045–1059.

[64] M.R. Sultana, B. Islam, S.R.A. Ahmed, Modeling and performance analysis of highly efficient copper indium gallium selenide solar cell with Cu_2O hole transport layer using solar cell capacitance simulator in one dimension, Phys. Status Solidi A 10 (2021), 2100512.

[65] S.R.A. Ahmed, M. Rahaman, A. Sunny, S. Rahman, M.S. Islam, T.A.E. Taha, Z.A. Alrowaili, M.S. Mian, Enhancing the efficiency of Cu_2Te thin-film solar cell with WS_2 buffer layer: a simulation study, Opt Laser. Technol. 159 (2023), 108942.

[66] S. Dridi, N. Bitri, S. Mahjoubi, F. Chaabouni, I. Ly, One-step spray of Cu_2NiSnS_4 thin films as absorber materials for photovoltaic applications, J. Mater. Sci. Mater. Electron. 31 (2020) 7193–7199.

[67] C. Rödl, A. Schleife, Photoemission spectra and effective masses of n- and p-type oxide semiconductors from first principles: ZnO, CdO, SnO_2, MnO, and NiO, Phys. Status Solidi 211 (2014) 74–81.

[68] A. Lenz, H. Kariis, A. Pohl, P. Persson, L. Ojamäe, The electronic structure and reflectivity of PEDOT:PSS from density functional theory, Chem. Phys. 384 (2011) 44–51.

[69] T.S. Sherkar, C. Momblona, L. Gil-Escrig, J. Ávila, M. Sessolo, H.J. Bolink, L.J.A. Koster, Recombination in perovskite solar cells: significance of grain boundaries, interface traps, and defect ions, ACS Energy Lett. 5 (2017) 1214–1222.

[70] Gagandeep Ritu, R. Kumar, F. Chand, Performance enhancement in $MA_{0.7}FA_{0.3}PbI_3$ based perovskite solar cell by gradient doping, Optik 274 (2023), 170558.

[71] N. Wang, Y. Zhou, M.-G. Ju, H.F. Garces, T. Ding, S. Pang, X.C. Zeng, N.P. Padture, X.W. Sun, Heterojunction-depleted lead-free perovskite solar cells with coarse-grained B-γ-$CsSnI_3$ thin films, Adv. Energy Mater. 6 (2016), 1601130.

[72] Q. Duan, J. Ji, X. Hong, Y. Fu, C. Wang, K. Zhou, X. Liu, H. Yang, Z.-Y. Wang, Design of hole-transport-material free $CH_3NH_3PbI_3/CsSnI_3$ all-perovskite heterojunction efficient solar cells by device simulation, Sol. Energy 201 (2020) 555–560.

[73] A. Ghosh, S. Dipta, S. Nikor, N. Saqib, A. Saha, Performance analysis of an efficient and stable perovskite solar cell and a comparative study of incorporating metal oxide transport layers, J. Opt. Soc. Am. B 37 (2020) 1966–1973.

[74] S. Zheng, G. Wang, T. Liu, L. Lou, S. Xiao, S. Yang, Materials and structures for the electron transport layer of efficient and stable perovskite solar cells, Sci. China Chem. 62 (2019) 800–809.

[75] S. Li, B. He, J. Xu, H. Lu, J. Jiang, J. Zhu, Z. Kan, L. Zhu, F. Wu, Highly efficient inverted perovskite solar cells incorporating P3CT-Rb as a hole transport layer to achieve a large open circuit voltage of 1.144 V, Nanoscale 12 (2020) 3686–3691.

[76] H. Xu, F. Yuan, D. Zhou, X. Liao, L. Chen, Y. Chen, Hole transport layers for organic solar cells: recent progress and prospects, J. Mater. Chem. A 8 (2020) 11478–11492.

[77] Y. Raouia, H. Ez-Zhraouy, N. Tahiri, O. El Bounaguid, S. Ahmad, S. Kazim, Performance analysis of $MAPbI_3$ based perovskite solar cells employing diverse charge selective contacts: simulation study, Sol. Energy 193 (2019) 948–955.

[78] J.Y. Kwak, Absorption coefficient estimation of thin MoS_2 film using attenuation of silicon substrate Raman signal, Results Phys. 13 (2019), 102202.

[79] K. Ali, Z. Ali, Analytical study of electrical performance of SiGe-based n^+-p-p^+ solar cells with $BaSi_2$ BSF structure, Sol. Energy 225 (2021) 91–96.

[80] D. Głowienka, D. Zhang, F.D. Giacomo, M. Najafi, S. Veenstra, J. Szmytkowski, Y. Galagan, Role of surface recombination in perovskite solar cells at the interface of $HTL/CH_3NH_3PbI_3$, Nano Energy 67 (2020), 104186.

[81] M. Matys, R. Stoklas, J. Kuzmik, B. Adamowicz, Z. Yatabe, T. Hashizume, Characterization of capture cross sections of interface states in dielectric/III-nitride heterojunction structures, J. Appl. Phys. 119 (2016), 205304.

[82] W. Isoe, M. Mageto, C. Maghanga, M. Mwamburi, V. Odari, C. Awino, Thickness dependence of window layer on $CH_3NH_3PbI_{3-X}Cl_X$ perovskite solar cell, Int. J. Photoenergy 2020 (2020), 8877744.

[83] L. Lin, P. Li, Z. Kang, H. Xiong, Y. Chen, Q. Yan, L. Jiang, Y. Qiu, Device Design of doping-controlled homojunction perovskite solar cells omitting HTL and exceeding 25% efficiency, Adv. Theory Simul. 4 (2021) 2000222.

[84] P. Singh, N.M. Ravindra, Temperature dependence of solar cell performance-an analysis, Sol. Energy Mater. Sol. Cells 101 (2012) 36–45.

[85] M.A. Rahman, Performance analysis of WSe_2-based bifacial solar cells with different electron transport and hole transport materials by SCAPS-1D, Heliyon 8 (2022), e09800.

[86] A. Hosen, M.S. Mian, S.R.A. Ahmed, Simulating the performance of a highly efficient $CuBi_2O_4$ based thin flm solar cell, SN Appl. Sci. 3 (2021) 544.

[87] A. Teyou Ngoupo, S. Ouédraogo, F. Zougmoré, J.M.B. Ndjaka, Numerical analysis of ultrathin Sb_2Se_3-based solar cells by SCAPS-1D numerical simulator device, Chin. J. Phys. 70 (2021) 1–13.

[88] H.B. Michaelson, The work function of the elements and its periodicity, J. Appl. Phys. 48 (1977) 4729–4733.

[89] F. Behrouznejad, S. Shahbazi, N. Taghavinia, H.-P. Wu, E.W.-G. Diau, A study on utilizing different metals as the back contact of $CH_3NH_3PbI_3$ perovskite solar cells, J. Mater. Chem. A 4 (2016) 13488–13498.

[90] S. Paul, S. Grover, I.L. Repins, B.M. Keyes, M.A. Contreras, K. Ramanathan, R. Noufi, Z. Zhao, F. Liao, J.V. Li, Analysis of back-contact interface recombination in thin-film solar cells, IEEE J. Photovoltaics 8 (2018) 871.

[91] A. Srivastava, S.K. Tripathy, T.R. Lenka, V. Goyal, Numerical simulations of novel quaternary chalcogenide $Ag_2MgSn(S/Se)_4$ based thin film solar cells using SCAPS 1-D, Sol. Energy 239 (2022) 337–349.

[92] A. Hosen, M.S. Mian, S.R.A. Ahmed, Improving the performance of lead-free $FASnI_3$-based perovskite solar cell with Nb_2O_5 as an electron transport layer, Adv. Theory Simul. 6 (2023), 2200652.